

Spectrally Adapted Physics-Informed Neural Networks for Solving Unbounded Domain Problems

Mingtao Xia

Dept. of Mathematics

UCLA

Los Angeles, CA 90095-1555, USA

XIAMINGTAO97@UCLA.EDU

Lucas Böttcher

Computational Social Science

Frankfurt School of Finance and Management

Frankfurt am Main, 60322, Germany

L.BOETTCHER@FS.DE

Tom Chou

Dept. of Mathematics

UCLA

Los Angeles, CA 90095-1555, USA

TOMCHOU@UCLA.EDU

Editor:

Abstract

Solving analytically intractable partial differential equations (PDEs) that involve at least one variable defined in an unbounded domain requires efficient numerical methods that accurately resolve the dependence of the PDE on that variable over several orders of magnitude. Unbounded domain problems arise in various application areas and solving such problems is important for understanding multi-scale biological dynamics, resolving physical processes at long time scales and distances, and performing parameter inference in engineering problems. In this work, we combine two classes of numerical methods: (i) physics-informed neural networks (PINNs) and (ii) adaptive spectral methods. The numerical methods that we develop take advantage of the ability of physics-informed neural networks to easily implement high-order numerical schemes to efficiently solve PDEs. We then show how recently introduced adaptive techniques for spectral methods can be integrated into PINN-based PDE solvers to obtain numerical solutions of unbounded domain problems that cannot be efficiently approximated by standard PINNs. Through a number of examples, we demonstrate the advantages of the proposed spectrally adapted PINNs (s-PINNs) over standard PINNs in approximating functions, solving PDEs, and estimating model parameters from noisy observations in unbounded domains.

Keywords: Physics-informed neural networks, PDE models, spectral methods, adaptive methods, unbounded domains

1. Introduction

The use of neural networks as universal function approximators (Hornik, 1991; Park et al., 2020) led to various applications in simulating (Raissi et al., 2019; Karniadakis et al., 2021) and controlling (Asikis et al., 2022; Böttcher et al., 2021; Lewis et al., 2020) physical, biological, and engineering systems. Training neural networks in function-approximation tasks

is typically realized in two steps. In the first step, an observable u_s associated with each distinct sample or measurement point $(x, t)_s \equiv (x_s, t_s)$, $s = 1, 2, \dots, n$ is used to construct the corresponding loss function (*e.g.*, the mean squared loss) in order to find representations for the constraint $u_s \equiv u(x_s, t_s)$ or infer the equations u obeys. In many physical settings, the variables x and t denote the space and time variables, respectively. Thus, the data points $(x, t)_s$ in many cases can be classified in two groups, $\{x_s\}$ and $\{t_s\}$, and the information they contain may be manifested differently in an optimization process. In the second step, the loss function is minimized by backpropagating gradients to adjust neural network parameters Θ . If the number of observations n are limited, additional constraints may help to make the training process more effective (Kukačka et al., 2017).

To learn and represent the dynamics of physical systems, physics-informed neural networks (PINNs) (Raissi et al., 2019; Karniadakis et al., 2021) provide one possible constraint on the training process. The key idea underlying PINN-based training is that the constraints imposed by the known equations of motion for some parts of the system are embedded in the loss function. Terms in the loss function associated with the differential equation can be evaluated using a neural network, which could be trained via backpropagation and automatic differentiation. In accordance with the distinction between Lagrangian and Hamiltonian formulations of the equations of motion in classical mechanics, physics-informed neural networks can be also divided into these two categories (Lutter et al., 2019; Roehrl et al., 2020; Zhong et al., 2019). Another formulation of PINNs uses variational principles (Kharazmi et al., 2019) in the loss function to further constrain the types of functions used. Such variational PINNs rely on finite element (FE) methods to discretize partial differential equation (PDE)-type constraints.

Many other PINN-based numerical algorithms have been recently proposed. A space-time domain decomposition PINN method was proposed for solving nonlinear PDEs (Jagtap and Karniadakis, 2020). In other variants, physics-informed Fourier neural operators have also been proposed to learn the underlying PDE models (Li et al., 2021). In general, PINNs link modern neural network methods with traditional complex physical models and allow algorithms to efficiently use higher-order numerical schemes to (i) solve complex physical problems with high accuracy, (ii) infer model parameters, and (iii) reconstruct physical models in data-driven inverse problems (Raissi et al., 2019). Therefore, PINNs have become increasingly popular as they are able to avoid certain computational difficulties encountered when using traditional FE/FD methods to find solutions to physics models.

The broad utility of PINNs is reflected in their application to aerodynamics (Mao et al., 2020), surface physics (Fang and Zhan, 2019), power systems (Misyris et al., 2020), cardiology (Sahli Costabal et al., 2020), and soft biological tissues (Liu et al., 2020). When implementing PINN algorithms to find functions in an unbounded system, the unbounded variables cannot be simply normalized, precluding reconstruction of solutions outside the range of data. Nonetheless, many problems in nature are associated with long-ranged potentials (Böttcher and Herrmann, 2021; Strub and Böttcher, 2019) (*i.e.*, unbounded spatial domains) and processes that are subject to algebraic damping (Barré et al., 2011) (*i.e.*, unbounded temporal domains), and thus need to be solved in unbounded domains. For example, to capture the oscillatory and decaying behavior at infinity of the solution to Schrödinger’s equation, efficient numerical methods are required in the unbounded domain

\mathbb{R} (Li et al., 2018). As another example, in structured cellular proliferation models in mathematical biology, efficient unbounded domain numerical methods are required to resolve a blow up in the cell size over several orders of magnitude (Xia et al., 2020; Xia and Chou, 2021). Finally, in solid-state physics, long-range interactions (Mengotti et al., 2011; Hügli et al., 2012) require algorithms tailored for unbounded domain problems to accurately simulate particle interactions over long distances.

Solving unbounded domain problems is thus a key challenge in various fields that cannot be addressed with standard PINN-based solvers. To efficiently solve PDEs in unbounded domains, we will treat the information carried by the x_s data using spectral decompositions of u in the x variable. Thus, we combine PINNs with spectral methods and propose a spectrally adapted PINN (s-PINN) method that can also utilize recently developed adaptive function expansions techniques (Xia et al., 2021a,b). Our approach will be distinct from that taken in standard PINN, variational-PINN, or physics-informed neural operator approaches. We do not input x into the network or try to learn $u(x)$ as a composition of, *e.g.*, Fourier neural operators; instead, we assume that the function can be approximated by a spectral expansion in x with appropriate basis functions. Rather than learning the explicit spatial dependence directly, we train neural network learn the time-dependent expansion coefficients. Our main conceptual contributions are (i) the integration of spectral methods with multi-output neural networks to approximate the spectral expansions of functions when partial information is available, (ii) the incorporation of recently developed adaptive spectral methods in our spectrally adapted PINNs (s-PINNs), and (iii) presenting explicit examples illustrating how s-PINNs can be used to solve unbounded domain problems, recover spectral convergence, and compute derivatives more efficiently than automatic differentiation. We show how s-PINNs provide a unified, easy-to-implement method for solving PDEs and performing parameter-inference given noisy observation data and how complementary adaptive spectral techniques can further improve efficiency, especially for solving problems in unbounded domains.

In Sec. 2, we show how neural networks can be combined with modern adaptive spectral methods to outperform standard neural networks in function approximation tasks. As a first application, we show in Sec. 3 how efficient PDE solvers can be derived from spectral PINN methods. In Sec. 4, we discuss another application that focuses on reconstructing underlying physical models and inferring model parameters given observational data. In Sec. 5, we summarize our work and discuss possible directions for future research. A summary of the main variables and parameters used in this study is given in Table 1.

2. Combining Spectral Methods with Neural Networks

In this section, we first introduce the basic features of function approximators that rely on neural networks and spectral methods designed to handle variables that are defined in unbounded domains. In a dataset (x_s, t_s, u_s) , $s \in \{1, \dots, n\}$, x_s are values of the sampled “spatial” variable x which can be defined in an unbounded domain. We will also assume that our problem is defined within a finite time horizon so that t_j are time points restricted to a bounded domain, and are thus normalizable. One central goal is to approximate the constraint $u_s := u(x_s, t_s)$ by computing the function $u(x, t)$ and the equation it obeys. Our key assumption is that the solution’s behavior in x can be represented by a spectral

Symbol	Definition
n	number of observations
N	spectral expansion order
N_H	number of intermediate layers in the neural network
H	number of neurons per layer
η	learning rate of stochastic gradient descent
Θ	neural network hyperparameters
K	order of the Runge–Kutta scheme
β	scaling factor of basis functions $\phi_{i,x_L}^\beta(x) := \phi_i(\beta(x - x_L))$
x_L	translation of basis functions $\phi_{i,x_L}^\beta := \phi_i(\beta(x - x_L))$
u_{N,x_L}^β	spectral expansion of order N generated by the neural network: $u_{N,x_L}^\beta = \sum_{i=0}^N w_{i,x_L}^\beta \phi_i(\beta(x - x_L))$
$\mathcal{F}(u_{N,x_L}^\beta)$	frequency indicator for the spectral expansion u_{N,x_L}^β
$\hat{\mathcal{H}}_{i,x_L}^\beta$	generalized Hermite function of order i , scaling factor β , and translation x_L
P_{N,x_L}^β	function space defined by the first $N+1$ generalized Hermite functions $P_{N,x_L}^\beta := \{\hat{\mathcal{H}}_{i,x_L}^\beta\}_{i=0}^N$
q	scaling factor (β) adjustment ratio
ν	threshold for adjusting the scaling factor β
ρ, ρ_0	threshold for increasing, decreasing N
γ	ratio for adjusting ρ

Table 1: **Overview of variables.** A list of the main variables and parameters used in this paper.

decomposition, while u 's behavior in t remains unknown and to be learned from the neural network. This is achieved by isolating the possibly unbounded spatial variables x from the bounded variables t by expressing u in terms of suitable basis functions in x with time-dependent weights. As indicated in Fig. 1(a), we approximate u_s using

$$u_s := u(x_s, t_s) \approx u_N(x_s, t_s) := \sum_{i=0}^N w_i(t_s) \phi_i(x_s), \quad (1)$$

where $\{\phi_i\}_{i=0}^N$ are suitable basis functions that can be used to approximate u in an unbounded domain (see Fig. 1(b) for a schematic of a basis function $\phi_i(x)$ that decays with x). Examples of such basis functions include, for example, the generalized Laguerre functions in \mathbb{R}^+ and the generalized Hermite functions in \mathbb{R} (Shen et al., 2011). In addition to being defined on an unbounded domain, spectral expansions allow high accuracy (Trefethen,

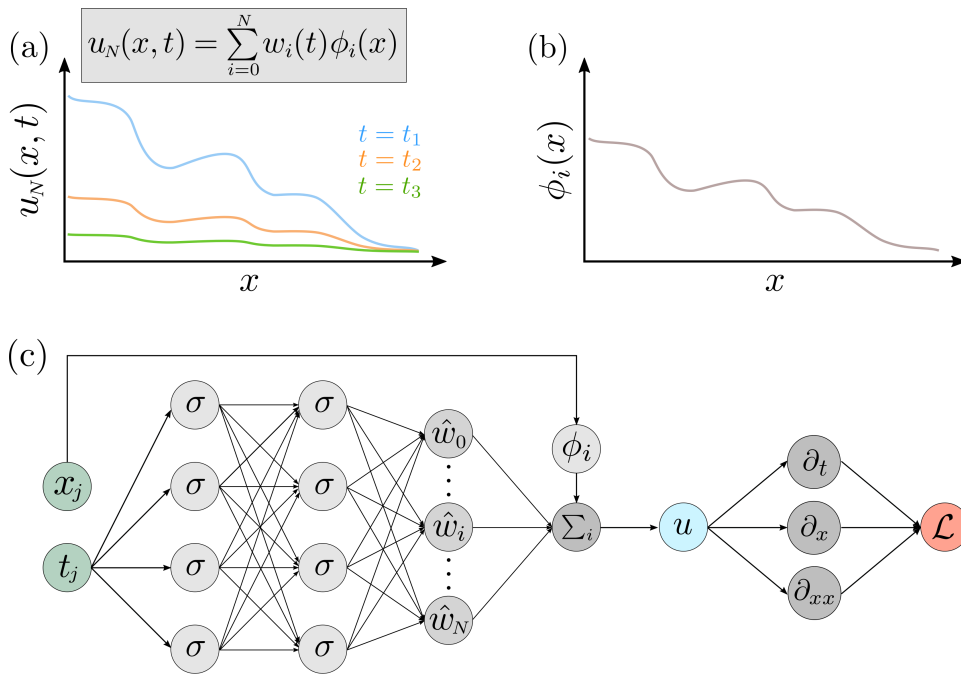


Figure 1: Solving unbounded domain problems with spectrally adapted physics-informed neural networks for functions $u_N(x, t)$ that can be expressed as a spectral expansion $u_N(x, t) = \sum_{i=0}^N w_i(t)\phi_i(x)$. (a) An example of a function $u_N(x, t)$ plotted at three different time points. (b) Decaying behavior of a corresponding basis function element $\phi_i(x)$. (c) PDEs in unbounded domains can be solved by combining spectral decomposition with the PINNs and minimizing the loss function \mathcal{L} . Spatial derivatives of basis functions are explicitly defined and easily obtained.

2000) calculations with errors that decay exponentially (spectral convergence) in space if the target function $u(x, t)$ is smooth.

Figure 1(c) shows a schematic of our proposed spectrally adapted PINN algorithm. The variable x is directly fed into the basis functions ϕ_i instead of being used as an input in the neural network. If one wishes to connect the output $u_N(x, t; \Theta)$ of the neural network to the solution of a PDE, one has to include derivatives of u with respect to x and t in the loss function \mathcal{L} . Derivatives that involve the variable x can be easily and explicitly calculated by taking derivatives of the basis functions with high accuracy while derivatives with respect to t can be obtained via automatic differentiation (Linnainmaa, 1976; Paszke et al., 2017).

If a function u can be written in terms of a spectral expansion in some dimensions (*e.g.*, x Eq. (1)) with appropriate spectral basis functions, we can approximate u using a multi-output neural network by solving the corresponding least squares optimization problem

$$\min_{\Theta} \left\{ \sum_s |u_N(x_s, t_s; \Theta) - u_s|^2 \right\}, \quad u_N(x, t; \Theta) = \sum_{i=0}^N w_i(t; \Theta)\phi_i(x), \quad (2)$$

where Θ is the hyperparameter set of a neural network that outputs the t -dependent vector of weights $w_i(t; \Theta)$. This representation will be used in the appropriate loss function depending on the application. The neural network can achieve arbitrarily high accuracy in the minimization of the loss function if it is deep enough and contains sufficient neurons in each layer (Hornik et al., 1989). Since the solution’s spatial behavior has been approximated by the spectral expansion which could achieve high accuracy with proper ϕ_i , we shall show that solving Eq. (2) can be more accurate and efficient than directly fitting to u_s by a neural network without using a spectral expansion.

As a motivating example, we compare the approximation error of a neural network which is fed both x_s and t_s with that of the s-PINN method in which only t_s are inputted, but with the information contained in x_s imposed on the solution via basis functions of x . We show that taking advantage of the prior knowledge on the x -data greatly improves training efficiency and accuracy. All neural networks that we use in our examples are based on fully connected linear layers with ReLU activation functions. Weights in each layer are initially distributed according to a uniform distribution $\mathcal{U}(-\sqrt{a}, \sqrt{a})$, where a is the inverse of the number of input features. To normalize hidden-layer outputs, we apply the batch normalization technique (Ioffe and Szegedy, 2015). Neural-network parameters are optimized using stochastic gradient descent.

Example 1: Function approximation

Consider approximating the function

$$u(x, t) = t \frac{8x \sin 3x}{(x^2 + 4)^2}, \tag{3}$$

which decays algebraically as $u(x \rightarrow \infty, t) \sim t/|x|^3$ when $|x| \rightarrow \infty$. To numerically approximate Eq. (3), we choose the loss function to be the mean-squared error

$$\text{MSE} = \frac{1}{n} \sum_{s=1}^n |u_N(x_s, t_s) - u_s|^2. \tag{4}$$

A standard neural network approach is applied by inputting *both* x_s and t_s into a 5-layer, 10 neuron-per-layer network defined by hyperparameters $\tilde{\Theta}$ to find a numerical approximation to $u_N(x_s, t_s) := \tilde{u}(x_s, t_s; \tilde{\Theta})$ by minimizing Eq. (4) with respect to $\tilde{\Theta}$ (the $\tilde{u}, \tilde{\Theta}$ notation refer to hyperparameters in the non-spectral neural network).

To apply a spectral multi-output neural network to this problem, we need to choose an appropriate spectral representation of the spatial dependence of Eq. (3), in the form of Eq. (2). In order to capture an algebraic decay at infinity as well as the oscillatory behavior resulting from the $\sin(3x)$ term, we start from the modified mapped Gegenbauer functions (MMGFs) (Tang et al., 2020)

$$R_i^{\lambda, \beta}(x) = (1 + (\beta x)^2)^{-(\lambda+1)/2} C_i^\lambda\left(\beta x / \sqrt{1 + (\beta x)^2}\right), \quad x \in \mathbb{R}, \tag{5}$$

where $C_i^\lambda(\cdot)$ is the Gegenbauer polynomial of order i . At infinity, the MMGFs decay as $R_i^{\lambda, \beta}(x) \sim \text{sign}(x)^i \frac{(2\lambda)_i}{i!} (1 + (\beta x)^2)^{-(\lambda+1)/2}$. A suitable basis ϕ_i needs to include functions that decay more slowly than x^{-3} . If we choose $\beta = 1/2$ and the special case $\lambda = 0$, the

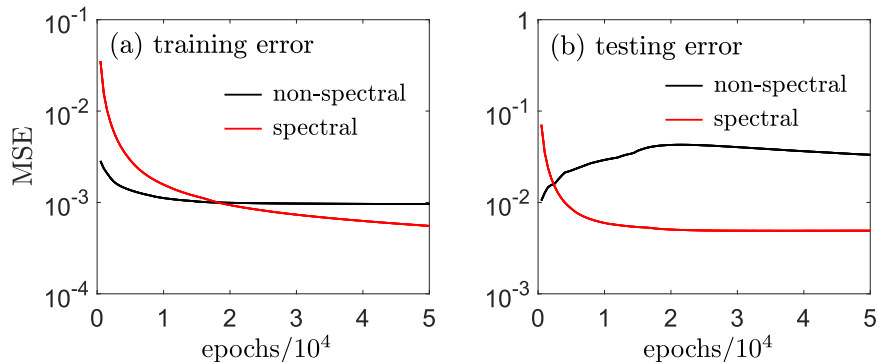


Figure 2: Example 1: **function approximation**. Approximation of the target function Eq. (3) using both standard neural-networks and a spectral multi-output neural network that learns the coefficients $w_i(t; \Theta)$ in the spectral expansion Eq. (1). Comparison of the approximation error using a spectral multi-output neural network (red) with the error incurred when using a standard neural-network function approximator (black). Here, both the spectral and non-spectral function approximators use the same number of parameters, but the spectral multi-output neural network converges much faster on the training set and has a smaller testing error than the standard neural network. (a) The training curve for the spectral multi-output neural network decreases much faster than that of the standard neural network. (b) Since the spectral multi-output neural network is better at fitting the data by taking advantage of the spectral expansion in x , its testing error is also much smaller and decreases faster.

basis function is defined as $\phi_i(x) = R_i^{0,\beta}(x) \equiv (1 + (\beta x)^2)^{-1/2} T_i(\beta x / \sqrt{1 + (\beta x)^2})$, where T_i are the Chebyshev polynomials. We thus use

$$u_N(x_s, t_s; \Theta) = \sum_{i=0}^{N=9} w_i(t_s; \Theta) R_i^{0,\beta}(x_s) \quad (6)$$

in Eq. (4) and use a 4-layer neural network with 10 neurons per layer to learn the coefficients $\{w_i(t; \Theta)\}_{i=0}^9$ by minimizing the MSE (Eq. (4)) with respect to Θ . The total numbers of parameters for both the 4-layer spectral multi-output neural network and the normal 5-layer neural network are the same. The training set and the testing set each contain $n = 200$ pairs of values $(x, t)_s = (x_s, t_s)$ where x_s are sampled from the Cauchy distribution, $x_s \sim \mathcal{C}(12, 0)$, and $t_s \sim \mathcal{U}(0, 1)$. For each pair (x_s, t_s) , we find $u_s = u(x_s, t_s)$ using Eq. (3). Clearly, x_s is sampled from the unbounded domain \mathbb{R} and cannot be normalized (the expectation and variance of the Cauchy distribution do not exist).

We set the learning rate $\eta = 5 \times 10^{-4}$ and plot the training and testing MSEs (Eq. 4) as a function of the number of training epochs in Fig. 2. Figures 2(a) and (b) show that the spectral multi-output neural network yields smaller errors since it naturally and efficiently captures the oscillatory and decaying feature of the underlying function u from Eq. (3). Directly fitting $u \approx \tilde{u}$ leads to over-fitting on the training set which does nothing to reduce the testing error. Therefore, it is important to take advantage of the data structure, in this case, using the spectral expansion to represent the function’s known oscillations and decay

as $x \rightarrow \infty$. In this and subsequent examples, all computations are performed using Python 3.8.10 on a laptop with a 4-core Intel[®] i7-8550U CPU @ 1.80 GHz.

3. Application to Solving PDEs

In this section, we show that spectrally adapted neural networks can be combined with physics-informed neural networks (PINNs) which we shall call spectrally adapted PINNs (s-PINNs). We apply s-PINNs to numerically solve PDEs, and in particular, PDEs in unbounded domains for which standard PINN approaches cannot be directly applied. Although we mainly focus on solving spatio-temporal problems, s-PINNs are also applicable to other types of PDEs.

Again, we assume the problem is defined over a finite time horizon t while the spatial variable x may be defined in an unbounded domain. Assuming the solution’s asymptotic behavior in x is known, we approximate it by a spectral expansion in x with suitable basis functions (*e.g.*, MMGFs in Example 1 for describing algebraic decay at infinity). However, the time dependence is unknown so we cannot simply use a spectral expansion in t and will need to forward time to solve for $u(x, t)$.

Assuming \mathcal{M} is an operator that only involves the spatial variable x (*e.g.*, ∂_x, ∂_x^2 , etc.), we can represent the solution to the spatio-temporal PDE $\partial_t u = \mathcal{M}[u](x, t)$ by the spectral expansion in Eq. (2) with expansion coefficients $\{w_i(t; \Theta)\}$ to be learned by a neural network with hyperparameters Θ .

As in standard PINNs, we use a high-order Runge–Kutta scheme to advance time by uniform timesteps Δt . What distinguishes our s-PINNs from standard PINNs is that only the intermediate times t_s between timesteps are defined as inputs to the neural network, while the outputs contain global spatial information (the spectral expansion coefficients), as shown in Fig. 1(c). Over a longer time scale, the optimal basis functions in the spectral expansion Eq. (2) may change. Therefore, one can use new adaptive spectral methods proposed in (Xia et al., 2021a,b). Using s-PINNs to solve PDEs has the advantages that they can (i) accurately represent spatial information via spectral decomposition, (ii) convert solving a PDE into an optimization and data fitting problem, (iii) easily implement high-order, implicit schemes to advance time with high accuracy, and (iv) allow the use of recently developed spectral-adaptive techniques that dynamically find the most suitable basis functions.

The approximated solution to the PDE $\partial_t u = \mathcal{M}[u](x, t)$ can be written at discrete timesteps $t_{j+1} - t_j = \Delta t$ as

$$u_N(x, t_{j+1}; \Theta_{j+1}) = \sum_{i=0}^N w_i(t_{j+1}; \Theta_{j+1}) \phi_i(x), \quad (7)$$

where $\Theta_{j+1}, j \geq 1$ is the hyperparameter set of the neural network used in the time interval $(j\Delta t, (j+1)\Delta t)$. In order to forward time from $t_j = j\Delta t$ to $t_{j+1} = (j+1)\Delta t$, we can use, *e.g.*, a K^{th} -order implicit Runge–Kutta scheme with $0 < c_s < 1$ ($s = 1, \dots, K$) the collocation points in time and a_{rs}, b_r ($r = 1, \dots, K$) the associated coefficients.

Given $u(x, t_j)$, the K^{th} order implicit Runge–Kutta scheme aims to approximate $u(x, t_j + c_s \Delta t)$ and $u(x, t_j + \Delta t)$ through

$$\begin{aligned} u_N(x, t_j + c_s \Delta t) &= u(x, t_j) + \sum_{r=1}^K a_{rs} \mathcal{M}[u_N(x, t_j + c_r \Delta t)], \\ u_N(x, t_j + \Delta t) &= u(x, t_j) + \sum_{r=1}^K b_r \mathcal{M}[u_N(x, t_j + c_r \Delta t)]. \end{aligned} \quad (8)$$

With the starting point $u_N(t_0, x; \Theta_0) := u_N(t_0, x)$ defined by the initial condition at t_0 , we define the target function as the sum of squared errors

$$\begin{aligned} \text{SSE}_j &= \sum_{s=1}^K \|u_N(x, t_j + c_s \Delta t; \Theta_{j+1}) - u_N(x, t_j; \Theta_j) - \sum_{r=1}^K a_{sr} \mathcal{M}[u_N(x, t_j + c_r \Delta t; \Theta_{j+1})]\|_2^2 \\ &\quad + \|u_N(x, t_j + \Delta t; \Theta_{j+1}) - u_N(x, t_j; \Theta_j) - \sum_{r=1}^K b_r \mathcal{M}[u_N(x, t_j + c_r \Delta t; \Theta_{j+1})]\|_2^2, \end{aligned} \quad (9)$$

where the L^2 norm is taken over the spatial variable x . Minimization of Eq. (9) provides a numerical solution at t_{j+1} given its value at t_j . If coefficients in the PDE are sufficiently smooth, we can use the basis function expansion in Eq. (7) for u_N and find that the weights at the intermediate Runge–Kutta time steps can be written as the Taylor expansion

$$w_i(t_j + c_r \Delta t; \Theta_j) = \sum_{\ell=0}^{\infty} \frac{w_i^{(\ell)}(t_j)}{\ell!} (c_r \Delta t)^\ell. \quad (10)$$

where $w_i^{(\ell)}(t_j)$ is the ℓ^{th} derivative of w_i with respect to time, evaluated at t_j . Therefore, the neural network is learning the mapping $t_j + c_s \Delta t \rightarrow \sum_{\ell=0}^{\infty} w_i^{(\ell)}(t_j) (c_s \Delta t)^\ell / \ell!$ for every i by minimizing the loss function Eq. (9).

Example 2: Solving bounded domain PDEs

Before focusing on the application of s-PINNs to PDEs whose solution is defined in an unbounded domain, we first consider the numerical solution of a PDE in a bounded domain to compare the performance of the spectral PINN method (using recently developed adaptive methods) to that of the standard PINN. Consider the following PDE:

$$\begin{aligned} \partial_t u &= \left(\frac{x+2}{t+1} \right) \partial_x u, \quad x \in (-1, 1), \\ u(x, 0) &= \cos(x+2), \quad u(1, t) = \cos(3(t+1)), \end{aligned} \quad (11)$$

which admits the analytical solution $u(x, t) = \cos((t+1)(x+2))$. In this example, we use Chebyshev polynomials $T_i(x)$ as basis functions and the corresponding Chebyshev–Gauss–Lobatto quadrature allocation points and weights such that the boundary $u(1, t) = \cos(3(t+1))$ can be directly imposed at an allocation point $x = 1$.

Since the solution becomes increasingly oscillatory in x over time, an ever-increasing expansion order (*i.e.*, the number of basis functions) is needed to accurately capture this

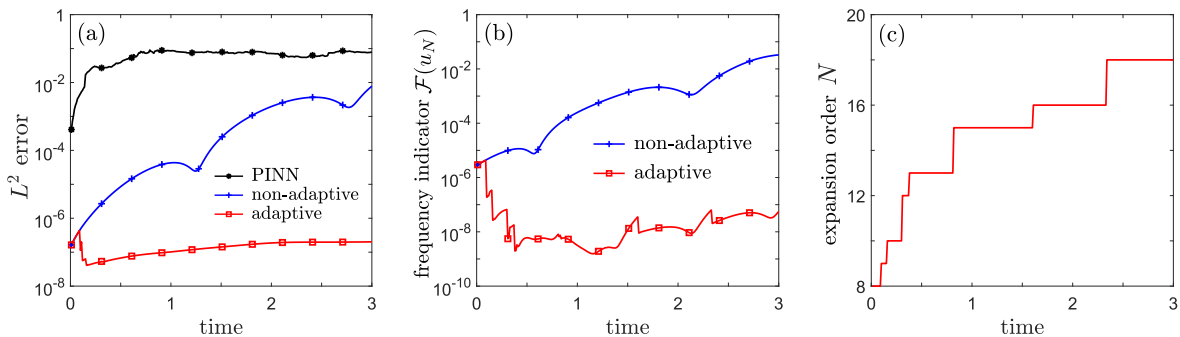


Figure 3: Example 2: **solving Eq. (11) in a bounded domain.** L^2 errors, frequency indicators, and expansion order associated with the numerical solution of Eq. (11) using the adaptive s-PINN method with a timestep $\Delta t = 0.01$. (a) In a bounded domain, the s-PINNs, with and without the adaptive spectral technique, have smaller errors than the standard PINN (black). Moreover, the s-PINN method combined with a p -adaptive technique that dynamically increases the number of basis functions (red) exhibits a smaller error than the non-adaptive s-PINN (blue). The higher accuracy of the adaptive s-PINN is a consequence of maintaining a small frequency indicator (12), as shown in (b). (c) Keeping the frequency indicator at small values is realized by increasing the spectral expansion order.

behavior. Between consecutive timesteps, we employ a recently developed p -adaptive technique for tuning the expansion order (Xia et al., 2021b). This method is based on monitoring and controlling a frequency indicator $\mathcal{F}(u_N)$ defined by

$$\mathcal{F}(u_N) = \left(\frac{\sum_{i=N-\lfloor \frac{N}{3} \rfloor + 1}^N \gamma_i (w_i)^2}{\sum_{i=0}^N \gamma_i (w_i)^2} \right)^{\frac{1}{2}}, \quad (12)$$

where $\gamma_i := \int_{-1}^1 (T_i)^2 (1-x^2)^{-1/2} dx$. The frequency indicator $\mathcal{F}(u_N)$ measures the proportion of high-frequency waves and serves as a lower error bound of the numerical solution $u_N(x, t; \Theta) := \sum_{i=0}^N w_i(t; \Theta) T_i(x)$. When $\mathcal{F}(u_N)$ exceeds its previous value by more than a factor ρ , the expansion order is increased by one. The indicator is then updated and the factor ρ also scaled by a parameter $\gamma \geq 1$.

We use a fourth-order implicit Runge–Kutta method to advance time in the SSE (9) and in order to adjust the expansion order in a timely way, we take $\Delta t = 0.01$. The initial expansion order $N = 8$, and the two parameters used to determine the threshold of adjusting the expansion order are set to $\rho = 1.5$ and $\gamma = 1.3$. A neural network with $N_H = 4$ layers and $H = 200$ neurons per layer is used in conjunction with the loss function (9) to approximate the solution of Eq. (11). We compare the results obtained using the s-PINN method with those obtained using a fourth-order implicit Runge–Kutta scheme with $\Delta x = \frac{1}{256}$, $\Delta t = 0.01$ in a standard PINN approach Raissi et al. (2019), also using $N_H = 4$ and $H = 200$.

Figure 3 shows that s-PINNs can be used to greatly improve accuracy because the spectral method can recover exponential convergence in space, and when combined with a high-order accurate implicit scheme in time, the overall error is small. In particular, the large error shown in Fig. (3) of the standard PINN suggests that the error of applying auto-differentiation to calculate the spatial derivative is significantly larger than the spatial derivatives calculated using spectral methods. Moreover, when equipping spectral PINNs with the p -adaptive technique to dynamically adjust the expansion order, the frequency indicator can be controlled, leading to even smaller errors as shown in Fig. 3(b,c).

Computationally, using our 4-core laptop on this example, the standard PINN method requires $\sim 10^6$ seconds while the s-PINN approach with and without adaptive spectral techniques (dynamically increasing the expansion order N) required 1711 and 1008 seconds, respectively. Thus, s-PINN methods can easily be computationally more efficient than the standard PINN approach. This advantage can be better understood by noting that training of standard PINNs requires time $\sim \mathcal{O}(\sum_{i=0}^{N_H} H_i H_{i+1})$ (H_i is the number of neurons in the i^{th} layer) to calculate each spatial derivative (e.g., $\partial_x u, \partial_x^2 u, \dots$) by autodifferentiation Baydin et al. (2018). However, in an s-PINN, since a spectral decomposition $u_N(x, t; \Theta)$ has been imposed, the computational time to calculate derivatives of all orders is $\mathcal{O}(N)$, where N is the expansion order. Since $\sum_{i=0}^{N_H} H_i H_{i+1} \geq \sum_{i=0}^{N_H} H_i$ and the total number of neurons $\sum_{i=0}^{N_H} H_i$ is usually much larger than the expansion order N , using s-PINNs can also reduce computational cost.

What distinguishes s-PINNs from the standard PINN framework is that the latter uses spatial and temporal variables as neural-network inputs, implicitly assuming that all variables are normalizable especially when batch-normalization techniques are applied in training a neural network. However, s-PINNs rely on spectral expansions to represent the dependence of a function $u(x, t)$ on the spatial variable x . Thus, x can be defined in unbounded domains and does not need to be normalizable. In the following example, we shall explore how our s-PINN is applied to solving a PDE defined in $(x, t) \in \mathbb{R}^+ \times [0, T]$.

Example 3: Solving unbounded domain PDEs

Consider the following PDE, which is similar to Eq. (11) but is defined in $(x, t) \in \mathbb{R}^+ \times [0, T]$:

$$\begin{aligned} \partial_t u &= - \left(\frac{x}{t+1} \right) \partial_x u, \\ u(x, 0) &= e^{-x}, \quad u(0, t) = 1. \end{aligned} \tag{13}$$

Equation (13) admits the analytical solution $u(x, t) = \exp[-x/(t+1)]$. In this example, we use the basis functions $\{\hat{\mathcal{L}}_i^\beta(x)\} := \{\hat{\mathcal{L}}_i^{(0)}(\beta x)\}$ where $\hat{\mathcal{L}}_i^{(0)}(x)$ is the generalized Laguerre function of order i defined in Shen et al. (2011). Here, we use the Laguerre-Gauss quadrature allocation nodes and weights so that $x = 0$ is *not* included in the allocation node set. We use a fourth-order implicit Runge-Kutta method to minimizing the SSE (9) by advancing time. In order to address the boundary condition, we augment the loss function

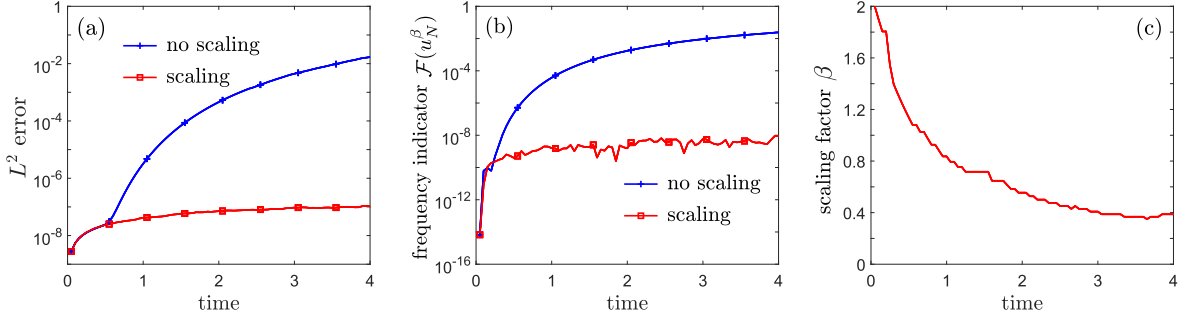


Figure 4: Example 3: **solving Eq. (13) in an unbounded domain.** L^2 error, frequency indicator, and expansion order associated with the numerical solution of Eq. (13) using the s-PINN method combined with the spectral scaling technique. (a) The s-PINN method with the scaling technique (red) has a smaller error than the s-PINN without scaling (blue). The higher accuracy of the adaptive s-PINN is a consequence of maintaining a smaller frequency indicator Eq. (12), as shown in (b). (c) Keeping the frequency indicator at small values is realized by reducing the scaling factor so that the basis functions decay more slowly at infinity. The timestep $\Delta t = 0.05$.

in Eq. (9) with terms that represent the cost of deviating from the boundary condition:

$$\begin{aligned}
 \text{SSE}_j = & \sum_{s=1}^K \|u_N(x, t_j + c_s \Delta t; \Theta_{j+1}) - u_N(x, t_j; \Theta_j) - \sum_{r=1}^K a_{sr} \mathcal{M}[u_N(x, t_j + c_r \Delta t; \Theta_{j+1})]\|_2^2 \\
 & + \|u_N(x, t_j + \Delta t; \Theta_{j+1}) - u_N(x, t_j; \Theta_j) - \sum_{r=1}^K b_r \mathcal{M}[u_N(x, t_j + c_r \Delta t; \Theta_{j+1})]\|_2^2 \\
 & + \sum_{s=1}^K [u_N(0, t_j + c_s \Delta t; \Theta_{j+1}) - u(0, t_j + c_s \Delta t)]^2 + [u_N(0, t_{j+1}; \Theta_{j+1}) - u(0, t_{j+1})]^2,
 \end{aligned} \tag{14}$$

where the last two terms pushes the constraints associated with the Dirichlet boundary condition at $x = 0$ at all time points:

$$u_N(0, t_j + c_s \Delta t; \Theta_{j+1}) = u(0, t_j + c_s \Delta t), \quad u_N(0, t_{j+1}; \Theta_{j+1}) = u(0, t_{j+1}), \tag{15}$$

where in this example, $u(0, t_j + c_s \Delta t) = u(0, t_{j+1}) \equiv 1$.

Because the solution of Eq. (13) becomes more diffusive with x (*i.e.* decays more slowly at infinity), it is necessary to decrease the scaling factor β to allow basis functions to decay more slowly at infinity. Between consecutive timesteps, we apply the scaling technique proposed in Xia et al. (2021a) to adjust the scaling factor. As with the p -adaptive technique we used in Example 2, the scaling technique also relies on monitoring and controlling the frequency indicator given in Eq. (12). In order to efficiently and dynamically tune the scaling factor, we take $\Delta t = 0.05$. The initial expansion order is $N = 8$, the initial scaling factor is $\beta = 2$, the scaling factor adjustment ratio is set to $q = 0.95$, and the threshold for tuning the scaling factor is set to $\nu = 1/(0.95)$. A neural network with 10 layers and 100 neurons per layer is used in conjunction with the loss function (9). The neural network of the

standard PINN consists of eight intermediate layers with 200 neurons per layer. Figure 4(a) shows that s-PINNs can achieve very high accuracy even when a relatively large timestep ($\Delta t = 0.05$) is used. Scaling techniques to dynamically control the frequency indicator are also successfully incorporated into s-PINNs, as shown in Figs. 3(b,c).

In Eq. (13), we imposed a Dirichlet boundary condition by modifying the SSE (14) to include boundary terms. Other types of boundary conditions can be applied in s-PINNs by including boundary constraints in the SSE as in standard PINN approaches.

In the next example, we focus on solving a PDE with two spatial variables, x and y , each defined in an unbounded domain.

Example 4: Solving higher dimensional unbounded domain PDEs

Consider the two-dimensional heat equation

$$\begin{aligned} \partial_t u(x, y, t) &= \Delta u(x, y, t), \quad (x, y) \in \mathbb{R}^2, \\ u(x, y, 0) &= \frac{1}{\sqrt{2}} e^{-x^2/4 - y^2/8}, \end{aligned} \tag{16}$$

which admits the analytical solution

$$u(x, y, t) = \frac{1}{\sqrt{(t+3)(t+2)}} \exp \left[-\frac{x^2}{4(t+3)} - \frac{y^2}{4(t+2)} \right]. \tag{17}$$

Note that the solution spreads out over time in both dimensions, *i.e.*, it decays more slowly at infinity as time increases. Therefore, we apply the scaling technique proposed in Xia et al. (2021a) to capture the increasing spread by adjusting the scaling factors β_x and β_y of the generalized Hermite basis functions. Generalized Hermite functions of orders $i = 0, \dots, N_x$ and $\ell = 0, \dots, N_y$ are used in the x and y directions, respectively.

In order to solve Eq. (16), we multiply it by any test function $v \in H^1(\mathbb{R})$ and integrate the resulting equation by parts to convert it to the weak form $(\partial_t u, v) = -(\nabla u, \nabla v)$. When implementing the spectral method, the goal is to find

$$u_{N_x, N_y}^{\beta_x, \beta_y}(x, y, t) = \sum_{i=0}^{N_x} \sum_{\ell=0}^{N_y} w_{i, \ell}(t) \hat{\mathcal{H}}_{i,0}^{\beta_x}(x) \hat{\mathcal{H}}_{\ell,0}^{\beta_y}(y), \tag{18}$$

where $\hat{\mathcal{H}}_{i,0}^{\beta_x}, \hat{\mathcal{H}}_{\ell,0}^{\beta_y}$ are generalized Hermite functions defined in Table 1 such that $(\partial_t u, v) = -(\nabla u, \nabla v)$ $t \in (t_j, t_{j+1})$ for all $v \in P_{N_x,0}^{\beta_x} \times P_{N_y,0}^{\beta_y}$, $t \in (t_j, t_{j+1})$. This allows one to advance time from t_j to t_{j+1} given $u_{N_x, N_y}^{\beta_x, \beta_y}(x, t_j)$.

Tuning the scaling factors β_x, β_y across different timesteps is achieved by monitoring the frequency indicators in the x - and y -directions, \mathcal{F}_x and \mathcal{F}_y , as detailed in (Xia et al., 2021a). We use initial expansion orders $N_x = N_y = 8$ and scaling factors $\beta_x = 0.4, \beta_y = 0.5$. The ratio and threshold for adjusting the scaling factors, are set to be $q = 0.95$ and $\nu^{-1} = 0.95$. The timestep $\Delta t = 0.1$ is used to adjust both scaling factors in both dimensions in timely manner and a fourth order implicit Runge–Kutta scheme is used for numerical integration. The neural network that we use to learn $w_{i, \ell}(t)$ has 13 intermediate layers with 80 neurons in each layer.

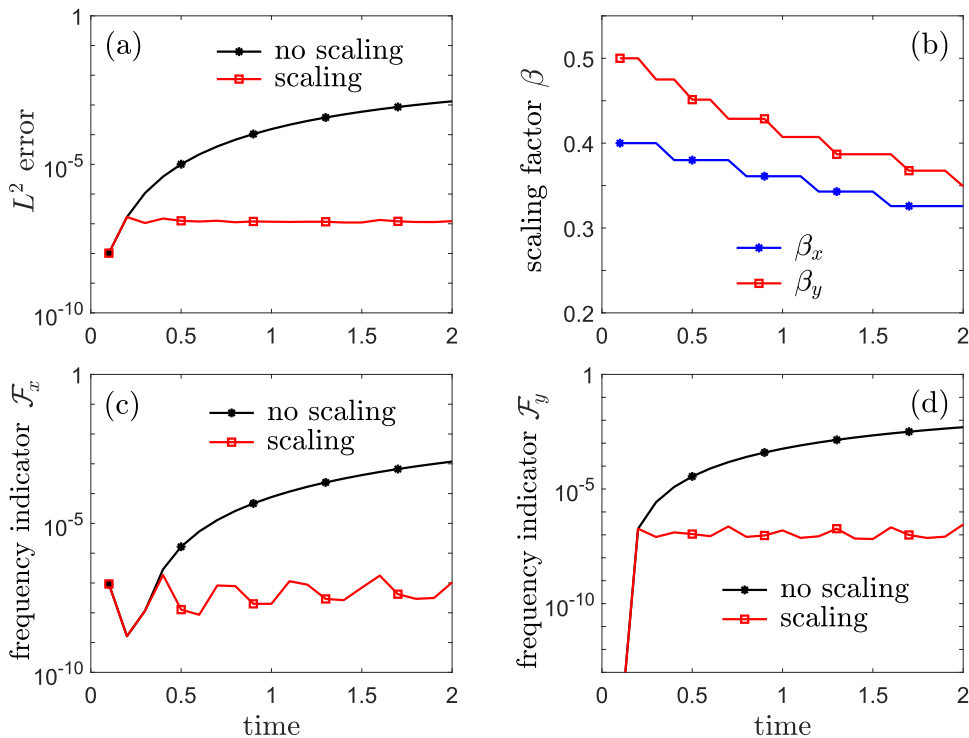


Figure 5: Example 4: **solving a higher dimensional unbounded domain PDE (Eq. (16))**. L^2 error, scaling factor, and frequency indicators associated with the numerical solution of Eq. (16) using s-PINNs, with and without dynamic scaling. (a) L^2 error as a function of time. The s-PINNs that are equipped with the scaling technique (red) achieve higher accuracy than those without (black). (b) The scaling factors β_x (blue) and β_y (red) as functions of time. Both scaling factors are decreased to match the spread of the solution in both the x and y directions. Scaling factors are adjusted to maintain small frequency indicators in the x -direction (c), and in the y -direction (d). The timestep $\Delta t = 0.1$.

The results depicted in Fig. 5(a) show that an s-PINN using the scaling technique can achieve high accuracy by using high-order Runge–Kutta schemes in minimizing the SSE (9) and by properly adjusting β_x and β_y (shown in Fig. 5(b)) to control the frequency indicators \mathcal{F}_x and \mathcal{F}_y (shown in Fig. 5(c) and (d)). The s-PINNs can be extended to higher spatial dimensions by calculating the numerical solution expressed in tensor product form as in Eq. (18). Additionally, a hyperbolic cross space Shen and Wang (2010) can be used to improve efficiency by reducing the necessary number of basis functions.

In the next example, we explore how s-PINNs can be used to solve Schrödinger’s equation in $x \in \mathbb{R}$. Solving this complex-valued equation poses substantial numerical difficulties as the solution exhibits diffusive, oscillatory, and convective behavior (Li et al., 2018).

Example 5: Solving an unbounded domain Schrödinger equation

We seek to numerically solve the following Schrödinger equation

$$\begin{aligned} i\partial_t\psi(x, t) &= -\partial_x^2\psi(x, t), \quad x \in \mathbb{R}, \\ \psi(x, 0) &= \frac{1}{\sqrt{\zeta}} \exp\left[ikx - \frac{x^2}{4\zeta}\right]. \end{aligned} \quad (19)$$

For reference, Eq. (19) admits the analytical solution

$$\psi(x, t) = \frac{1}{\sqrt{\zeta + it}} \exp\left[ik(x - kt) - \frac{(x - 2kt)^2}{4(\zeta + it)}\right]. \quad (20)$$

As in Example (4), we shall numerically solve Eq. (19) in the weak form

$$(\partial_t\Psi(x, t), v) + i(\partial_x\Psi(x, t), \partial_x v) = 0, \quad \forall v \in H^1(\mathbb{R}). \quad (21)$$

Since the solution to Eq. (19) decays as $\sim \exp[-x^2/(4\sqrt{(\zeta^2 + t^2)})]$ at infinity, we shall use the generalized Hermite functions as basis functions. The solution was shown in Xia et al. (2021b) to be rightward-translating for $k > 0$ and increasingly oscillatory and spread-out over time. Hence, as detailed in Xia et al. (2021a), we apply three additional adaptive spectral techniques to improve efficiency and accuracy: (i) a scaling technique to adjust the scaling factor β over time in order to capture diffusive behavior, (ii) a moving technique to adjust the center of the basis function x_L to capture convective behavior, and (iii) a p -adaptive technique to increase the number of basis functions N to better capture the oscillations. We set the initial parameters $\beta = 0.8, x_L = 0, N = 24$ at $t = 0$. The scaling factor adjustment ratio and the threshold for adjusting the scaling factor are $q = \nu^{-1} = 0.95$, the minimum and maximum displacements are 0.004 and 0.1 within each timestep for moving the basis functions, respectively, and the threshold for moving is 1.001. Finally, the thresholds of the p -adaptive technique are set to $\rho = \rho_0 = 2$ and $\gamma = 1.4$. To numerically solve Eq. (21), a fourth-order implicit Runge–Kutta scheme is applied to advance time with timestep $\Delta t = 0.1$. The neural network underlying the s-PINN that we use in this example contains 13 layers with 80 neurons in each layer. Figure 6(a) shows that the s-PINN with adaptive spectral techniques leads to very high accuracy as it is able to properly adjust the basis functions over a longer timescale (across different timesteps), while not adapting the basis functions results in larger errors. Figs. 6(b–d) show that the scaling factor β decreases over time to match the spread of the solution, the displacement of the basis function x_L increases in time to capture the rightward movement of the basis functions, and the expansion order N increases to capture the solution’s increasing oscillatory behavior. Our results indicate that our s-PINN method can effectively utilize all three adaptive algorithms.

We now explore how the timestep and the order of the implicit Runge–Kutta method affect the approximation error, *i.e.*, to what extent can we relax the constraint on the timestep and maintain the accuracy of the basis functions, or, if higher-order Runge–Kutta schemes are better. Another feature to explore is neural network structure, such as the number of layers and neurons per layer, and how it affects the performance of s-PINNs. In the following example, we carry out a sensitivity analysis.

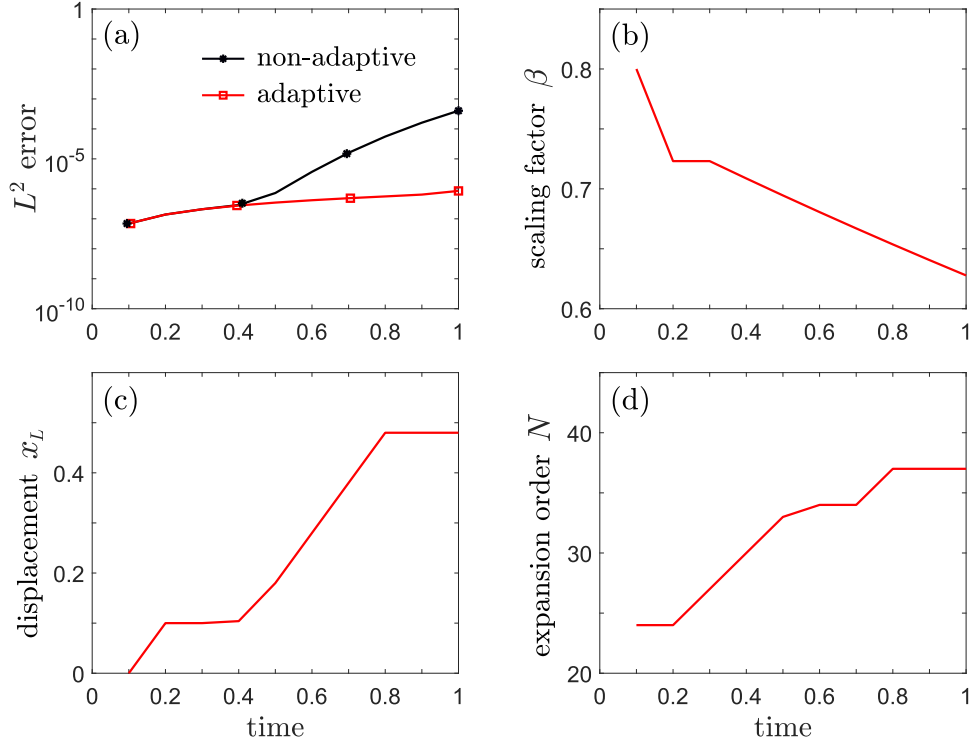


Figure 6: Example 5: **solving the Schrödinger equation (Eq. (19)) in an unbounded domain.** Approximation error, scaling factor, displacement, and expansion order associated with the numerical solution of Eq. (19) using adaptive (red) and non-adaptive (black) s-PINNs. (a) Errors for numerically solving Eq. (19) with and without adaptive techniques. (b) The change of the scaling factor which decreases over time as the solution becomes more spread out. (c) The displacement of the basis functions x_L which is increased as the solution moves rightwards. (d) The expansion order N increases over time as the solution becomes more oscillatory. The timestep $\Delta t = 0.1$.

Example 6: Sensitivity analysis of s-PINN

To explore how the performance of an s-PINN depends on algorithmic set-up and parameters, we apply it to solving the heat equation

$$\begin{aligned} \partial_t u(x, t) &= \partial_x^2 u(x, t) + f(x, t), \quad x \in \mathbb{R}, \\ u(x, 0) &= e^{-x^2/4} \sin x \end{aligned} \quad (22)$$

using generalized Hermite functions as basis functions. For the source $f(x, t) = [x \cos x + (t + 1) \sin x] (t + 1)^{-3/2} \exp[-\frac{x^2}{4(t+1)}]$, Eq. (22) admits the analytical solution

$$u(x, t) = \frac{\sin x}{\sqrt{t+1}} \exp\left[-\frac{x^2}{4(t+1)}\right]. \quad (23)$$

Table 2: Example 6: **sensitivity analysis of s-PINN**. Errors, the final scaling factors, and the computational run-time for different timesteps Δt and different implicit order- K Runge–Kutta schemes. In each box, the run-time (in seconds), the SSE, and the final scaling factor are listed from left to right. The results associated with the smallest error are highlighted in red while the results associated with shortest run-time are indicated in blue.

$\Delta t \backslash K$	2	4	6	10
0.02	885, 6.851e-09, 0.545	1081, 5.934e-09, 0.545	3070, 2.533e-07, 0.545	23585, 6.458e-05, 0.591
0.05	544, 2.378e-08, 0.545	370, 1.474e-08, 0.545	1784, 2.566e-07, 0.545	9438, 1.040e-06, 0.545
0.1	262, 2.613e-06, 0.681	128, 2.606e-06, 0.681	259, 2.624e-06, 0.681	3814, 2.855e-06, 0.681
0.2	92, 3.761e-06, 0.695	83, 2.087e-06, 0.695	110, 2.109e-06, 0.695	3089, 4.430e-06, 0.709

We solve Eq. (22) in the weak form by multiplying any test function $v \in H^1(\mathbb{R})$ on both sides and integrating by parts to obtain

$$(\partial_t u, v) = -(\partial_x u, \partial_x v) + (f, v), \quad \forall v \in H^1(\mathbb{R}). \quad (24)$$

The solution diffusively spreads over time, requiring one to decrease the scaling factor β of the generalized Hermite functions $\{\mathcal{H}_i^\beta(x)\}$. We shall first study how the timestep and the order of the implicit Runge–Kutta method associated with solving the minimization problem (9) affect our results. A neural network with 13 layers, 100 neurons per layer, and a learning rate $\eta = 5 \times 10^{-4}$ is used and the scaling factor is set to $\beta = 0.8$ at $t = 0$.

Table 2 shows that, since the error from temporal discretization Δt^{2K} is already quite small for $K \geq 4$, using a higher-order Runge–Kutta method does significantly improve accuracy for all choices of Δt . Moreover, using higher-order ($K \geq 4$) schemes tends to require longer run-times. Higher orders require fitting over more data points (using the same number of parameters) leading to slower convergence when minimizing Eq. (9).

In Table 2, we marked the smallest run-time in blue and the smallest error in red, which both occur for $K = 4$. However, both the error and the computational cost tend to decrease when we increase the order K from 2 to 4, indicating that a second-order implicit Runge–Kutta method could be insufficient to keep the time discretization error small, thus requiring longer times to converge. Additionally, the error always increases with Δt regardless of the order of the Runge–Kutta scheme. However, the expected convergence order is not observed, implying that the increase in error results from lagging adjustment of the scaling factor β when Δt is too large, rather than from an insufficiently small-time discretization error Δt^{2K} . Finally, the computational cost increases linearly with Δt . Using a fourth-order implicit Runge–Kutta scheme with $\Delta t = 0.05$ to solve Eq. (24) seems to both achieve high accuracy and avoid large computational costs.

We also investigate how the total number of parameters in the neural network and the structure of the network affect efficiency and accuracy. We use a sixth-order implicit Runge–Kutta scheme with $\Delta t = 0.1$. The learning rate is set to $\eta = 5 \times 10^{-4}$ for all neural networks.

As shown in Table 3, the computational cost tends to decrease with both the number of neurons in each layer H and the number of layers N_H . We observe that with more neurons

Table 3: Example 6: **sensitivity analysis of s-PINN**. Errors, the final scaling factors, and the run-time for different numbers of intermediate layers N_H and neurons per layer H . In each box, the run-time (in seconds), the SSE, and the final scaling factor are listed from left to right. Results associated with the smallest error are marked in red while those associated with the shortest run-time are highlighted in blue.

$N_H \backslash H$	3	5	8	13
50	2501, 8.884e-03, 0.628	3624, 5.503e-04, 0.603	4006, 7.313e-04, 0.591	3484, 5.443e-04, 0.641
80	2773, 6.850e-04, 0.695	2883, 3.569e-07, 0.545	2930, 1.140e-06, 0.603	1387, 2.567e-07, 0.545
100	3926, 3.780e-04, 0.695	1723, 2.567e-07, 0.545	1563, 2.567e-07, 0.545	1129, 2.566e-07, 0.545
200	3010, 2.569e-07, 0.545	728, 2.566e-07, 0.545	1252, 1.195e-07, 0.545	1006, 2.567e-07, 0.545

in each layer and more layers, it takes fewer epochs to converge when minimizing Eq. (9). We marked the shortest run-time in blue and the smallest error in red, which both arise when $H = 200$. The errors when $H = 50$ are significantly larger as the training terminates (after a maximum of 40000 epochs) before it converges. For $N_H = 3$, the corresponding s-PINN always fails to achieve accuracy within 40000 epochs unless $H \gtrsim 200$. Therefore, overparametrization is indeed helpful in improving the neural network’s performance, leading to faster convergence rates, in contrast to most traditional optimization methods that take longer to converge with more parameters. Similar observations have been made in other optimization tasks that involve deep neural networks (Arora et al., 2018; Chen et al., 2020). Consequently, the s-PINN method retains advantages of deep and wide neural networks for improving accuracy and efficiency.

4. Parameter Inference and Source Reconstruction

As with standard PINN approaches, s-PINNs can also be used for parameter inference in PDE models or even for reconstructing unknown sources in a physical model. Assuming observational data at uniform time intervals $t_j = j\Delta t$ associated with a partially known underlying PDE model, s-PINNs can be trained to infer model parameters θ by minimizing the sum of squared errors, weighted from both ends of the time interval (t_j, t_{j+1}) ,

$$\text{SSE}_j = \text{SSE}_j^L + \text{SSE}_j^R, \tag{25}$$

where

$$\begin{aligned} \text{SSE}_j^L &= \sum_{s=1}^K \|u(x, t_j + c_s \Delta t; \theta_{j+1}; \Theta_{j+1}) - u(x, t_j; \theta_j) \\ &\quad - \sum_{r=1}^K a_{sr} \mathcal{M}[u(x, t_j + c_r \Delta t; \theta_{j+1}; \Theta_{j+1})]\|_2^2, \\ \text{SSE}_j^R &= \sum_{s=1}^K \|u(x, t_j + c_s \Delta t; \theta_{j+1}; \Theta_{j+1}) - u(x, t_{j+1}; \theta_{j+1}) \\ &\quad - \sum_{r=1}^K (a_{sr} - b_r) \mathcal{M}[u(x, t_j + c_r \Delta t; \theta_{j+1}; \Theta_{j+1})]\|_2^2. \end{aligned} \tag{26}$$

Here, θ_{j+1} is the model parameter to be found using the sample points $c_s\Delta t$ between t_j and t_{j+1} . The most obvious advantage of s-PINNs over standard PINN methods is that they can deal with models defined on unbounded domains, extending PINN-based methods that are typically applied to finite domains.

Given observations over a certain time interval, one may wish to both infer parameters θ_j in the underlying physical model and reconstruct the solution u at any given time. Here, we provide an example in which both a parameter in the model is to be inferred and the numerical solution obtained.

Example 7: Parameter (diffusivity) inference

As a starting point for a parameter-inference problem, we consider diffusion with a source term

$$\begin{aligned}\partial_t u(x, t) &= \kappa \partial_x^2 u(x, t) + f(x, t), \quad x \in \mathbb{R} \\ u(x, 0) &= e^{-x^2/4} \sin x,\end{aligned}\tag{27}$$

where the constant parameter κ is the thermal conductivity (or diffusion coefficient) in the entire domain. In this example, we set $\kappa = 2$ as a reference and assume the source

$$f(x, t) = \left[\frac{2(x \cos x + (t+1) \sin x)}{(t+1)^{3/2}} - \frac{x^2}{4(t+1)^2} + \frac{\sin x}{2(t+1)^{3/2}} \right] \exp \left[-\frac{x^2}{4(t+1)} \right].\tag{28}$$

In this case, the analytical solution to Eq. (27) is given by Eq. (23). We numerically solve Eq. (27) in the weak form as Eq. (24). From observations taken at discrete time points $t_j = j\Delta t$, we wish to reconstruct the parameter κ in Eq. (27) (e.g., the thermal conductivity) and obtain the numerical solutions at $t_j + c_s\Delta t$ in Eq. (25) by minimizing Eq. (26).

Here, a neural network with 13 layers and 100 neurons per layer is used with a sixth-order implicit Runge–Kutta scheme. The timestep Δt is 0.1. At each time step, we draw the function values from

$$u(x, t_j) = \frac{\sin x}{\sqrt{t_j+1}} \exp \left[-\frac{x^2}{4(t_j+1)} \right] + \xi, \quad \xi \sim \mathcal{N}(0, \sigma^2).\tag{29}$$

where $\mathcal{N}(0, \sigma^2)$ is the normal distribution of mean 0 and variance σ^2 . We are interested in how different levels of noise ξ and the increasing spread of the solution will affect the SSE and the reconstructed parameter $\hat{\kappa}$. Figure 7 shows the error of the reconstructed $\hat{\kappa}$, $|\hat{\kappa} - 2|$, the SSE, the scaling factor, and the frequency indicator as functions of time for different noise levels. Figure 7(a) shows that the larger the noise, the less accurate the reconstructed κ . Moreover, as the function becomes more spread out (when $\sigma^2 = 0$), the error in both the reconstructed diffusivity and the SSE increases across time, as shown in Fig. 7(b). This behavior suggests that a diffusive solution that decays more slowly at infinity can give rise to inaccuracies in the numerical computation of the intermediate timestep solutions and in reconstructing model parameters. Finally, larger variances in the noise will impede the scaling process since the frequency indicator cannot be as easily controlled since larger variance in the noise usually corresponds to high-frequency and oscillatory components of a solution, as indicated in Fig. 7(c,d).

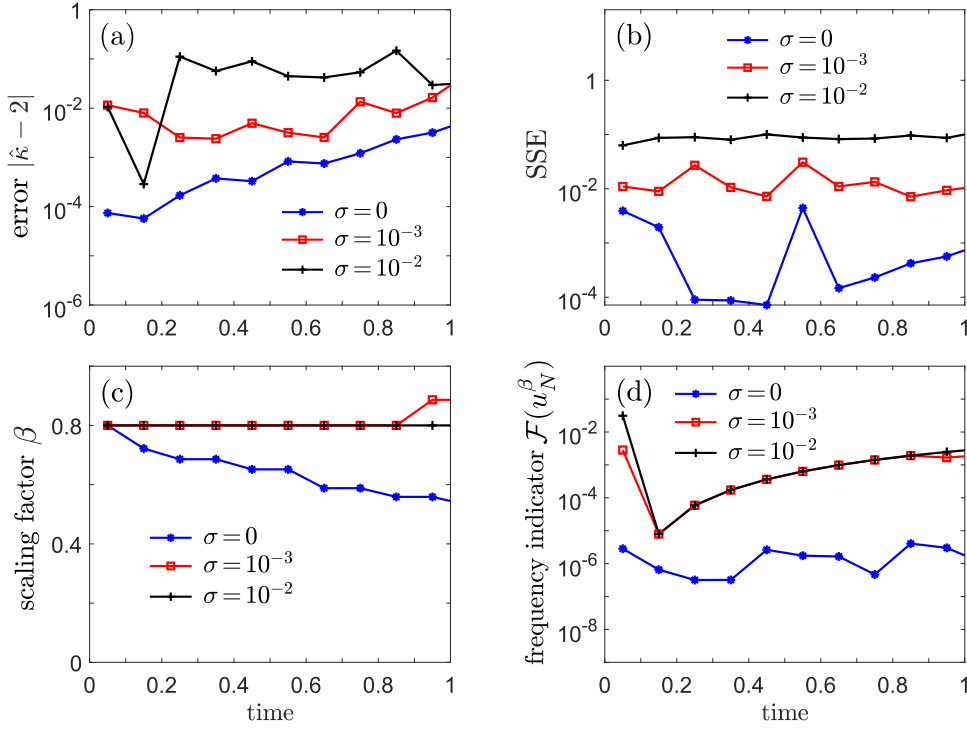


Figure 7: Example 7: **parameter (diffusivity) inference**. The parameter κ inferred within successive time windows of $\Delta t = 0.1$, the SSE error Eq. (25), the scaling factor, and the frequency indicators associated with solving Eq. (27), for different noise levels σ^2 . Here, the SSE was minimized to find the estimate $\hat{\theta} \equiv \hat{\kappa}$ and the solutions u_N at intermediate timesteps $t_j + c_s \Delta t$. (a, b) Smaller σ^2 leads to smaller SSE Eq. (26) and a more accurate reconstruction of $\hat{\kappa}$. When the function has spread out significantly at long times, the reconstructed $\hat{\kappa}$ becomes less accurate, suggesting that unboundedness and small function values render the problem susceptible to numerical difficulties. (c, d) Noisy data results in a larger proportion of high-frequency waves and thus a large frequency indicator, impeding proper scaling.

In example 7, both the parameter and the unknown solution were inferred. Apart from reconstructing the coefficients in a given physical model, in certain applications, we may also wish to reconstruct the underlying physical model by inferring, *e.g.*, the heat source $f(x, t)$. Source recovery from observational data commonly arises and has been the subject of many previous studies (Yan et al., 2009; Yang et al., 2011; Yang and Fu, 2010). We now discuss how the s-PINN methods presented here can also be used for this purpose. For example, in Eq. (22) or Eq. (27), we may wish to reconstruct an unknown source $f(x, t)$ by also approximating it with a spectral decomposition

$$f(x, t) \approx f_N(x, t) = \sum_{i=0}^N h_i(t) \phi_{i, x_L}^\beta(x), \quad (30)$$

and minimizing an SSE that is augmented by a penalty on the coefficients $h_i, i = 0, \dots, N$.

We learn the expansion coefficients h_i within $[t_j, t_{j+1}]$ by minimizing

$$\begin{aligned}
 \text{SSE}_j &= \text{SSE}_j^L + \text{SSE}_j^R + \lambda \sum_{s=1}^K \|\mathbf{h}_N(t_j + c_s \Delta t)\|_2^2, \quad \lambda \geq 0, \\
 \text{SSE}_j^L &= \sum_{s=1}^K \|u(x, t_j + c_s \Delta t) - u(x, t_j) \\
 &\quad - \sum_{r=1}^K a_{sr} [\partial_{xx} u(x, t_j + c_r \Delta t) + f_N(x, t_j + c_r \Delta t; \Theta_{j+1})]\|_2^2, \\
 \text{SSE}_j^R &= \sum_{s=1}^K \|u(x, t_j + c_s \Delta t) - u(x, t_{j+1}) \\
 &\quad - \sum_{r=1}^K (a_{sr} - b_r) [\partial_{xx} u(x, t_j + c_r \Delta t) + f_N(x, t_j + c_r \Delta t; \Theta_{j+1})]\|_2^2,
 \end{aligned} \tag{31}$$

where $\mathbf{h}_N(t_j + c_s \Delta t) \equiv (h_1(t_j + c_s \Delta t), \dots, h_N(t_j + c_s \Delta t))$. In this example, u (or the spectral expansion coefficients w_i of u) is assumed to be known at all intermediate time points $c_s \Delta t$ in (t_j, t_{j+1}) .

The last term in Eq. (31) adds an L^2 penalty term on the coefficients of f which tends to reconstruct smoother and smaller-magnitude sources as λ is increased. Other forms of regularization such as L^1 can also be considered (Wu and Tegmark, 2019). In the presence of noise, an L^1 regularization further drives small expansion weights to zero, yielding an inferred source f_N described by fewer nonzero weights.

Since the reconstructed heat source f_N is expressed in terms of a spectral expansion in Eq. (30), and minimizing the loss function Eq. (31) depends on the global information of the observation u , f at any location x also contains global information intrinsic to u . In other words, for such inverse problems, the s-PINN approach extracts global spatial information and is thus able to reconstruct global quantities. We consider an explicit case in the next example.

Example 8: Source recovery

Consider the canonical source reconstruction problem (Cannon, 1968; Johansson and Lesnic, 2007; Hasanov and Pektacc, 2014) of finding $f(x, t)$ in the heat equation model in Eq. (22) for which observational data are given by Eq. 29 but evaluated at $t_j + c_s \Delta t$. A physical interpretation of the reconstruction problem is identifying the heat source $f(x, t)$ using measurement data in conjunction with Eq. (22). As in Example 5, we numerically solve the weak form Eq. (24). To study how the L^2 penalty term in Eq. (31) affect source recovery and whether increasing the regularization λ will make the inference of f more robust against noise, we minimize Eq. (25) for different values of λ and σ^2 .

We use a neural network with 13 layers and 100 neurons per layer to reconstruct $f_i(t)$ in the decomposition Eq. (30) with $N = 16$, *i.e.*, the neural network outputs the coefficients th_i at the intermediate timesteps $t_j + c_s \Delta t$. The basis functions $\phi_{i, x_L}^\beta(x)$ are chosen to be Hermite functions $\hat{\mathcal{H}}_{i, x_L}^\beta(x)$. For simplicity, we consider the problem only at times within the first time point $[0, 0.2]$ and a fixed scaling factor $\beta = 0.8$ as well as a fixed displacement $x_L = 0$.

Table 4: The error SSE_0 from Eq. (26) and the error of the reconstructed source Eq. (32), under different strengths of data noise and regularization coefficients λ . The SSE is listed in the upper-right of each cell and the error of the reconstructed source (Eq. (32)) is listed in the lower-left of each cell.

$\sigma \backslash \lambda$	0	10^{-3}	10^{-2}	10^{-1}
0	0.1370 / 1.543e-08	0.1370 / 1.368e-05	0.1477 / 0.00132	0.3228 / 0.0888
10^{-3}	0.1821 / 2.837e-06	0.1818 / 2.736e-05	0.1702 / 1.387e-03	0.3222 / 0.08964
10^{-2}	1.0497 / 0.001517	1.0383 / 1.579e-03	0.8031 / 6.078e-03	0.3434 / 0.1168
10^{-1}	11.505 / 0.2976	11.458 / 0.3032	8.2961 / 0.6905	1.3018 / 2.9330

In Table 4, we record the L^2 error

$$\|f(x, t) - \sum_{i=0}^{16} h_i(t) \hat{\mathcal{H}}_{i, x_L}^\beta(x)\|_2 \quad (32)$$

the lower-left of each entry and the SSE_0 in the upper-right. Observe that as the variance of the noise increases, the reconstruction of f via the spectral expansion becomes increasingly inaccurate. In the noise-free case, taking $\lambda = 0$ in Eq. (31) achieves the smallest SSE_0

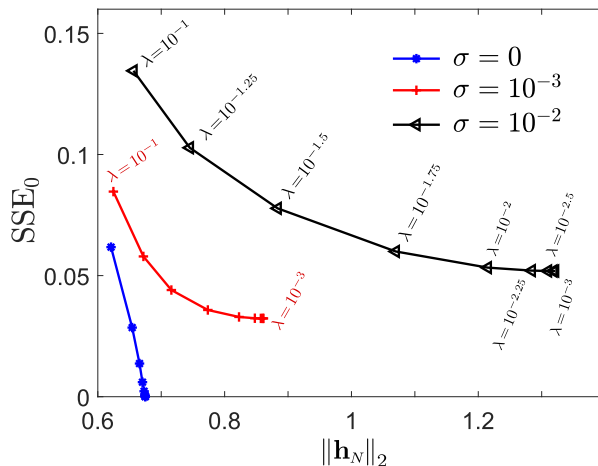


Figure 8: Example 8: **source recovery**. SSE_0 plotted against the reconstructed heat source $\|\mathbf{h}_N\|_2$ as given by (31), as a function of λ for various values of σ^2 (an “L-curve”). When λ is large, the norm of the reconstructed heat source $\|\mathbf{h}_N\|_2$ always tends to decrease while the “error” SSE_0 tends to increase. When $\lambda = 10^{-1}$, $\|\mathbf{h}_N\|_2$ is small and the SSE_0 is large. A moderate $\lambda \in [10^{-2}, 10^{-3}]$ could reduce the error SSE_0 , compared to using a large λ , while also generating a heat source with smaller $\|\mathbf{h}_N\|_2$.

and the smallest reconstruction error. However, with increasing noise σ^2 , using an L^2 regularization term in Eqs. (31) can prevent over-fitting of the data although SSE_0 increases

with the regularization strength λ . When $\sigma = 10^{-3}$, taking $\lambda = 10^{-2}$ achieves the smallest reconstruction error Eq. (32); when $\sigma = 10^{-2}, 10^{-1}$, $\lambda = 10^{-1}$ achieves the smallest reconstruction error. However, if λ is too large, coefficients of the spectral approximation to f are pushed to zero. Thus, it is important to choose an intermediate λ so that the reconstruction of the source is robust to noise. In Fig. 8, we plot the norm of the reconstructed heat source $\|\mathbf{h}_N\|_2$ and the “error” SSE_0 which varies as λ changes for different σ .

5. Summary and Conclusion

In this paper, we propose an approach that blends standard PINN algorithms with adaptive spectral methods and show through examples that this hybrid approach can be applied to a wide variety of data-driven problems including function approximation, solving PDEs, parameter inference, and model selection. The underlying feature that we exploit is the physical differences across classes of data. For example, by understanding the difference between space and time variables in a PDE model, we can describe the spatial dependence in terms of basis functions, obviating the need to normalize spatial data. Thus, s-PINNs are ideal for solving problems in unbounded domains. The only additional “prior” needed is an assumption on the asymptotic spatial behavior and an appropriate choice of basis functions. Additionally, adaptive techniques have been recently developed to further improve the efficiency and accuracy (Xia et al., 2021a,b), making spectral decomposition especially suitable for unbounded-domain problems that the standard PINN cannot easily address.

We applied s-PINNs (exploiting adaptive spectral methods) across a number of examples and showed that they can outperform simple neural networks for function approximation and existing PINNs for solving certain PDEs. Three major advantages are that the s-PINNs can be applied to unbounded domain problems, be more accurate by recovering spectral convergence in space, and be more efficient as a result of faster evaluation of spatial derivatives of all orders compared to standard PINNs that use autodifferentiation. These advantages are rooted in separated data structures, allowing for spectral computation and high-accuracy numerics. Moreover, the straightforward implementation of s-PINNs, which retain all the deep-neural-network learning features of PINNs, makes them ideal for data-driven inference problems.

In Table 5, we compare the advantages and disadvantages of the standard PINN and s-PINN methods. Potential improvements and extensions include applying techniques for selecting basis functions that best characterize the expected underlying process, spatial or otherwise, and inferring forms of the underlying model PDEs (Long et al., 2018; Raissi, 2018). While standard PINN methods deal with local information (*e.g.*, $\partial_x u, \partial_x^2 u$), spectral decompositions capture global information making them a natural choice for also efficiently learning and approximating nonlocal terms such as convolutions and integral kernels. Finally, one can incorporate a recently proposed Bayesian-PINN (B-PINN) (Yang et al., 2021) method into our s-PINN method to quantify uncertainty when solving inverse problems under noisy data.

Solvers Methods	Traditional	PINN
Non-spectral	<ul style="list-style-type: none"> + leverages existing numerical methods + low-order FD/FE schemes easily implemented + efficient evaluation of function and derivatives - mainly restricted to bounded domains - complicated implementation of higher-order schemes - algebraic convergence, less accurate - more complicated temporal and spatial extrapolation - requires understanding of problem to choose suitable discretization 	<ul style="list-style-type: none"> + easy implementation + efficient deep-neural-network training + easy extrapolation - mainly restricted to bounded domains - less accurate - less interpretable spatial derivatives - limited control of spatial discretization - expensive evaluation of neural networks - incompatible with existing numerical methods
Spectral	<ul style="list-style-type: none"> + suitable for bounded and unbounded domains + spectral convergence in space, more accurate + leverage existing numerical methods + efficient evaluation of function and derivatives - information required for choosing basis functions - more complicated implementation - more complicated temporal extrapolation - usually requires a “regular” domain <i>e.g.</i> rectangle, \mathbb{R}^d, a ball, etc. 	<ul style="list-style-type: none"> + suitable for both bounded and unbounded domains + easy implementation + spectral convergence in space, more accurate + efficient deep-neural-network training + more interpretable derivatives of spatial variables + easy extrapolation + compatible with existing adaptive techniques - requires some information to choose basis functions - expensive evaluation of neural networks - usually requires a “regular” domain

Table 5: **Advantages and disadvantages of traditional and PINN-based numerical solvers.** We use “+” and “-” signs to indicate advantages and disadvantages, respectively. Finite difference (FD), finite-element (FE), and spectral methods can be used in a traditional sense without relying on neural networks. This table provides an overview of the advantages and disadvantages associated with the corresponding methods and solvers.

Acknowledgments

LB acknowledges financial support from the Swiss National Fund (grant number P2EZP2_191888). The authors also acknowledge support from the US Army Research Office (W911NF-18-1-0345) and the National Science Foundation (DMS-1814364).

References

- Sanjeev Arora, Nadav Cohen, and Elad Hazan. On the optimization of deep networks: Implicit acceleration by overparameterization. In Jennifer Dy and Andreas Krause, editors, *Proceedings of the 35th International Conference on Machine Learning*, volume 80 of *Proceedings of Machine Learning Research*, pages 244–253, 2018.
- Thomas Asikis, Lucas Böttcher, and Nino Antulov-Fantulin. Neural ordinary differential equation control of dynamics on graphs. *Physical Review Research (in press)*, 2022.
- Julien Barré, Alain Olivetti, and Yoshiyuki Y Yamaguchi. Algebraic damping in the one-dimensional Vlasov equation. *Journal of Physics A: Mathematical and Theoretical*, 44(40):405502, 2011.
- Atilim Gunes Baydin, Barak A Pearlmutter, Alexey Andreyevich Radul, and Jeffrey Mark Siskind. Automatic differentiation in machine learning: a survey. *Journal of Machine Learning Research*, 18, 2018.
- Lucas Böttcher and Hans J Herrmann. *Computational Statistical Physics*. Cambridge University Press, 2021.
- Lucas Böttcher, Nino Antulov-Fantulin, and Thomas Asikis. AI Pontryagin or how neural networks learn to control dynamical systems. *Nature Communications*, 2021.
- John Rozier Cannon. Determination of an unknown heat source from overspecified boundary data. *SIAM Journal on Numerical Analysis*, 5(2):275–286, 1968.
- Zixiang Chen, Yuan Cao, Difan Zou, and Quanquan Gu. How much over-parameterization is sufficient to learn deep ReLU networks? In *International Conference on Learning Representations*, 2020.
- Zhiwei Fang and Justin Zhan. A physics-informed neural network framework for PDEs on 3D surfaces: Time independent problems. *IEEE Access*, 8:26328–26335, 2019.
- Alemdar Hasanov and Burhan Pektacc. A unified approach to identifying an unknown spacewise dependent source in a variable coefficient parabolic equation from final and integral overdeterminations. *Applied Numerical Mathematics*, 78:49–67, 2014.
- Kurt Hornik. Approximation capabilities of multilayer feedforward networks. *Neural Networks*, 4(2):251–257, 1991.
- Kurt Hornik, Maxwell Stinchcombe, and Halbert White. Multilayer feedforward networks are universal approximators. *Neural Networks*, 2(5):359–366, 1989.

- RV Hügli, G Duff, B O’Conchuir, E Mengotti, A Fraile Rodríguez, F Nolting, LJ Heyderman, and HB Braun. Artificial Kagomé spin ice: dimensional reduction, avalanche control and emergent magnetic monopoles. *Philosophical Transactions of the Royal Society A: Mathematical, Physical and Engineering Sciences*, 370(1981):5767–5782, 2012.
- Sergey Ioffe and Christian Szegedy. Batch normalization: Accelerating deep network training by reducing internal covariate shift. In *International Conference on Machine Learning*, pages 448–456. PMLR, 2015.
- Ameya D Jagtap and George Em Karniadakis. Extended physics-informed neural networks (XPINNs): A generalized space-time domain decomposition based deep learning framework for nonlinear partial differential equations. *Communications in Computational Physics*, 28(5):2002–2041, 2020.
- B Tomas Johansson and Daniel Lesnic. A variational method for identifying a spacewise-dependent heat source. *IMA Journal of Applied Mathematics*, 72(6):748–760, 2007.
- George Em Karniadakis, Ioannis G Kevrekidis, Lu Lu, Paris Perdikaris, Sifan Wang, and Liu Yang. Physics-informed machine learning. *Nature Reviews Physics*, 3(6):422–440, 2021.
- Ehsan Kharazmi, Zhongqiang Zhang, and George Em Karniadakis. Variational physics-informed neural networks for solving partial differential equations. *arXiv preprint arXiv:1912.00873*, 2019.
- Jan Kukačka, Vladimir Golkov, and Daniel Cremers. Regularization for deep learning: A taxonomy. *arXiv preprint arXiv:1710.10686*, 2017.
- FW Lewis, Suresh Jagannathan, and Aydin Yesildirak. *Neural network control of robot manipulators and non-linear systems*. CRC Press, 2020.
- Buyang Li, Jiwei Zhang, and Chunxiong Zheng. Stability and error analysis for a second-order fast approximation of the one-dimensional Schrödinger equation under absorbing boundary conditions. *SIAM Journal on Scientific Computing*, 40(6):A4083–A4104, 2018.
- Zongyi Li, Hongkai Zheng, Nikola Kovachki, David Jin, Haoxuan Chen, Burigede Liu, Kamyar Azizzadenesheli, and Anima Anandkumar. Physics-informed neural operator for learning partial differential equations. *arXiv preprint arXiv:2111.03794*, 2021.
- Seppo Linnainmaa. Taylor expansion of the accumulated rounding error. *BIT Numerical Mathematics*, 16(2):146–160, 1976.
- Minliang Liu, Liang Liang, and Wei Sun. A generic physics-informed neural network-based constitutive model for soft biological tissues. *Computer methods in applied mechanics and engineering*, 372:113402, 2020.
- Zichao Long, Yiping Lu, Xianzhong Ma, and Bin Dong. PDE-net: Learning PDEs from data. In *International Conference on Machine Learning*, pages 3208–3216. PMLR, 2018.

- M Lutter, C Ritter, and Jan Peters. Deep Lagrangian networks: Using physics as model prior for deep learning. In *International Conference on Learning Representations*. OpenReview.net, 2019.
- Zhiping Mao, Ameya D Jagtap, and George Em Karniadakis. Physics-informed neural networks for high-speed flows. *Computer Methods in Applied Mechanics and Engineering*, 360:112789, 2020.
- Elena Mengotti, Laura J Heyderman, Arantxa Fraile Rodríguez, Frithjof Nolting, Remo V Hügli, and Hans-Benjamin Braun. Real-space observation of emergent magnetic monopoles and associated Dirac strings in artificial Kagomé spin ice. *Nature Physics*, 7(1):68–74, 2011.
- George S Misyris, Andreas Venzke, and Spyros Chatzivasileiadis. Physics-informed neural networks for power systems. In *2020 IEEE Power & Energy Society General Meeting (PESGM)*, pages 1–5. IEEE, 2020.
- Sejun Park, Chulhee Yun, Jaeho Lee, and Jinwoo Shin. Minimum width for universal approximation. In *International Conference on Learning Representations*, 2020.
- Adam Paszke, Sam Gross, Soumith Chintala, Gregory Chanan, Edward Yang, Zach DeVito, Zeming Lin, Alban Desmaison, Luca Antiga, and Adam Lerer. Automatic differentiation in pytorch. 2017.
- Maziar Raissi. Deep hidden physics models: Deep learning of nonlinear partial differential equations. *Journal of Machine Learning Research*, 19(1):932–955, 2018.
- Maziar Raissi, Paris Perdikaris, and George E Karniadakis. Physics-informed neural networks: A deep learning framework for solving forward and inverse problems involving nonlinear partial differential equations. *Journal of Computational Physics*, 378:686–707, 2019.
- Manuel A Roehrl, Thomas A Runkler, Veronika Brandtstetter, Michel Tokic, and Stefan Obermayer. Modeling system dynamics with physics-informed neural networks based on Lagrangian mechanics. *IFAC-PapersOnLine*, 53(2):9195–9200, 2020.
- Francisco Sahli Costabal, Yibo Yang, Paris Perdikaris, Daniel E Hurtado, and Ellen Kuhl. Physics-informed neural networks for cardiac activation mapping. *Frontiers in Physics*, 8:42, 2020.
- Jie Shen and Li-Lian Wang. Sparse spectral approximations of high-dimensional problems based on hyperbolic cross. *SIAM Journal on Numerical Analysis*, 48(3):1087–1109, 2010.
- Jie Shen, Tao Tang, and Li-Lian Wang. *Spectral methods: algorithms, analysis and applications*, volume 41. Springer Science & Business Media, 2011.
- Stefan H Strub and Lucas Böttcher. Modeling deformed transmission lines for continuous strain sensing applications. *Measurement Science and Technology*, 31(3):035109, 2019.

- Tao Tang, Li-Lian Wang, Huifang Yuan, and Tao Zhou. Rational spectral methods for PDEs involving fractional Laplacian in unbounded domains. *SIAM Journal on Scientific Computing*, 42(2):A585–A611, 2020.
- Lloyd N Trefethen. *Spectral methods in MATLAB*. SIAM, 2000.
- Tailin Wu and Max Tegmark. Toward an artificial intelligence physicist for unsupervised learning. *Physical Review E*, 100(3):033311, 2019.
- Mingtao Xia and Tom Chou. Kinetic theory for structured populations: application to stochastic sizer-timer models of cell proliferation. *Journal of Physics A: Mathematical and Theoretical*, 2021.
- Mingtao Xia, Chris D Greenman, and Tom Chou. PDE models of adder mechanisms in cellular proliferation. *SIAM Journal on Applied Mathematics*, 80(3):1307–1335, 2020.
- Mingtao Xia, Sihong Shao, and Tom Chou. Efficient scaling and moving techniques for spectral methods in unbounded domains. *SIAM Journal on Scientific Computing*, 43(5):A3244–A3268, 2021a.
- Mingtao Xia, Sihong Shao, and Tom Chou. A frequency-dependent p-adaptive technique for spectral methods. *Journal of Computational Physics*, 446:110627, 2021b.
- Liang Yan, Feng-Lian Yang, and Chu-Li Fu. A meshless method for solving an inverse spacewise-dependent heat source problem. *Journal of Computational Physics*, 228(1):123–136, 2009.
- Fan Yang and Chu-Li Fu. A simplified Tikhonov regularization method for determining the heat source. *Applied Mathematical Modelling*, 34(11):3286–3299, 2010.
- Liu Yang, Mehdi Dehghan, Jian-Ning Yu, and Guan-Wei Luo. Inverse problem of time-dependent heat sources numerical reconstruction. *Mathematics and Computers in Simulation*, 81(8):1656–1672, 2011.
- Liu Yang, Xuhui Meng, and George Em Karniadakis. B-PINNs: Bayesian physics-informed neural networks for forward and inverse PDE problems with noisy data. *Journal of Computational Physics*, 425:109913, 2021.
- Yaofeng Desmond Zhong, Biswadip Dey, and Amit Chakraborty. Symplectic ODE-net: Learning Hamiltonian dynamics with control. In *International Conference on Learning Representations*, 2019.